

# Understanding the Long-Term Tidal Modulation on Methane Bubble Emissions Using Acoustics, Southern Hydrate Ridge, Cascadia

Bing Yu Lee<sup>1,2\*</sup>, Susan L. Hautala<sup>2</sup>

<sup>1</sup>Department of Geoinformation, Faculty of Built Environment and Surveying, Universiti Teknologi Malaysia, 81310 Skudai Johor, Malaysia. <sup>2</sup>School of Oceanography, University of Washington, Seattle, WA 98195, United States.

Corresponding email: bingyu0612@gmail.com

---

*Abstract* — Carbon output from methane hydrate in the seafloor reservoir likely plays an important role in global warming and is not well quantified. Our study investigates the temporal discontinuity of methane bubble emissions at Southern Hydrate Ridge (SHR), developing a proxy for the presence of bubble plumes based on a 3.5-month record of acoustic Doppler current profiler echo intensity from the Ocean Observatories Initiative Cabled Array. We find significant tidal modulation of bubble emissions, consistent with the promotion or inhibition of hydraulic fracturing by hydrostatic pressure changes in the water column. The bubbling behaviour at SHR is best explained by a tidally modulated dynamic equilibrium regulated from above by water column hydrostatic pressure and below by changes in pore fluid pressure at the base of the methane hydrate stability zone.

*Keywords* - Gas Hydrate, Southern Hydrate Ridge, Acoustic Doppler Current Profiler

©2021 Penerbit UTM Press. All rights reserved.

Article History: Received 22 December 2020, Accepted 13 April 2021, Published 1 August 2021

*How to cite:* Lee, Y.B., Hautala, S.L. (2021). Understanding the Long-Term Tidal Modulation on Methane Bubble Emissions Using Acoustics, Southern Hydrate Ridge, Cascadia. *Journal of Advanced Geospatial Science & Technology* 1(1), 70-88.

## 1. Introduction

Recently, methane hydrate has gained global attention for both its potential as an energy resource and its potential to drive climate change. With increasing global energy demands and depletion of oil and gas reserves, methane hydrate has emerged as a cleaner alternative energy resource (National Research Council 2010). Worldwide distribution of methane hydrate and the compound's high energy density of gas volume make methane hydrate a promising energy resource before the carbon-free age (Beaudoin et al., 2014 and Liu et al., 2019). On the other hand, hydrate degassing, which releases methane into the hydrosphere and atmosphere, could exacerbate global warming and marine extinction (Archer 2007; Johnson et al., 2015; Katz et al., 2001 and Liu et al., 2019). Because of its importance for future energy and climate change, scientific research related to methane hydrate has been conducted in 82 countries around the world (Liu et al., 2019).

Methane hydrate is an ice-like compound that forms as methane and water combine under low-temperature and high pressure, in which methane is concentrated within the molecular framework of a frozen water molecule (Ruppel, 2011 and Solomon et al., 2008). As the most prevalent kind of gas hydrate (~99%) found worldwide (Liu et al., 2019), methane hydrate can only form within the methane hydrate stability zone (MHSZ) limited by the ideal temperature and pressure for its formation (Ruppel, 2011). As a result, more than 99% of the global inventory of methane hydrate occurs in marine continental margins with high organic content (Liu et al., 2019).

The contribution of methane seeps to the global ocean carbon budget is poorly constrained despite methane hydrate's importance in global warming and marine extinction. Owing to methane's potency – 70 times that of carbon dioxides over 20 years – as greenhouse gas, it is widely accepted that hydrate degassing exacerbated paleoclimate warming (Archer 2007; Johnson et al., 2015; Katz et al., 2001 and Liu et al., 2019). During the Paleocene-Eocene Thermal Maximum, chronic and catastrophic methane release (Archer, 2007) may have been responsible for causing (1) a temperature increase of 4 to 6 °C in the deep sea and high latitude surface water (Katz et al., 2001), and (2) anoxia in the near-bottom water linked to the disappearance of ~55% of the foraminiferal taxa (Johnson et al., 2015 and Katz et al., 2001). Although preliminary estimates suggest methane seeps' contribution of 5 to 10 % of the global atmospheric carbon budget (Etiope and Milkov 2004), precise quantification of the carbon output from methane seeps has remained a challenge. Causes of the challenge include our limited understanding of the complex gas-hydrate derived methane seepage system (Liu et al.,

2019) and the discontinuous spatial and temporal distributions of methane seepage around the world (Johnson et al., 2015 and Riedel et al., 2018).

Our study focuses on the temporal discontinuity of methane bubble emissions from an active seep site at approximately 800-m depth below the sea level located about 90 km offshore of Newport, Oregon — Southern Hydrate Ridge (Figure 1.). SHR is an extensively studied site, part of the National Science Foundation’s Ocean Observatory Initiative (OOI) cabled array. Located along the Cascadia subduction margin, SHR comprises organic-rich sediments on the subducting oceanic plate that were scraped off, folded and faulted into an accretionary ridge (Johnson et al., 2006 and Tréhu et al., 2006). As the organic materials in the sediments are utilized by methanotrophic microbes, methane saturation occurs within the sediment pores and methane hydrate can form within the MHSZ (Riedel et al., 2018). At SHR, the base of MHSZ is located approximately 120 to 150 m below the seafloor (Bangs, Musgrave, and Trehu 2005). In this geological setting, methane hydrate is highly susceptible to dissociation due to the narrow MHSZ (Ruppel 2011) and could potentially be triggered by either an increase in the seafloor temperature due to warming (Hautala et al., 2014 and Johnson et al., 2015), or disruption of the seafloor stress system due to slope failure, erosion, earthquakes (Katz et al., 2001) and tides (Römer et al., 2016; Torres et al., 2002 and Tryon et al., 1999). When methane hydrate dissociates, methane gas can dissolve in the pore waters and subsequently be trapped within the sediments or delivered to the shallow ocean and atmosphere as bubbles (McGinnis et al., 2006).

Methane bubble emissions at SHR are hypothesized to be controlled by the local hydraulic fracturing system (Daigle, Bangs, and Dugan 2011). Within the porous medium below the base of MHSZ, methane gas can be trapped due to reduced permeability resulting from hydrate-filled fractures. At a depth of 15 to 20 m below the base of MHSZ, 2-4-m-thick coarse-grained turbidites have been found acting as permeable conduits that allow methane gas to be supplied to the shallow seafloor. As methane gas accumulates following methane hydrate dissociation near the base of MHSZ, pore pressure builds up within the sediment. When pore pressure exceeds the effective overlying stress exerted by the overlying sediments and water column, fractures would form allowing methane bubbles to seep into the ocean.

Although some studies have suggested potential tidal influence on methane bubble emissions (Torres et al., 2002 and Tyron et al., 1999), methane bubble emission behavior at SHR is still not well understood, with previous work not finding a clear relationship between tides and bubble emissions. Instead, bubble emission behavior at SHR has been characterized as transient and episodic (Philip et al., 2016a and Riedel et al., al. 2018).

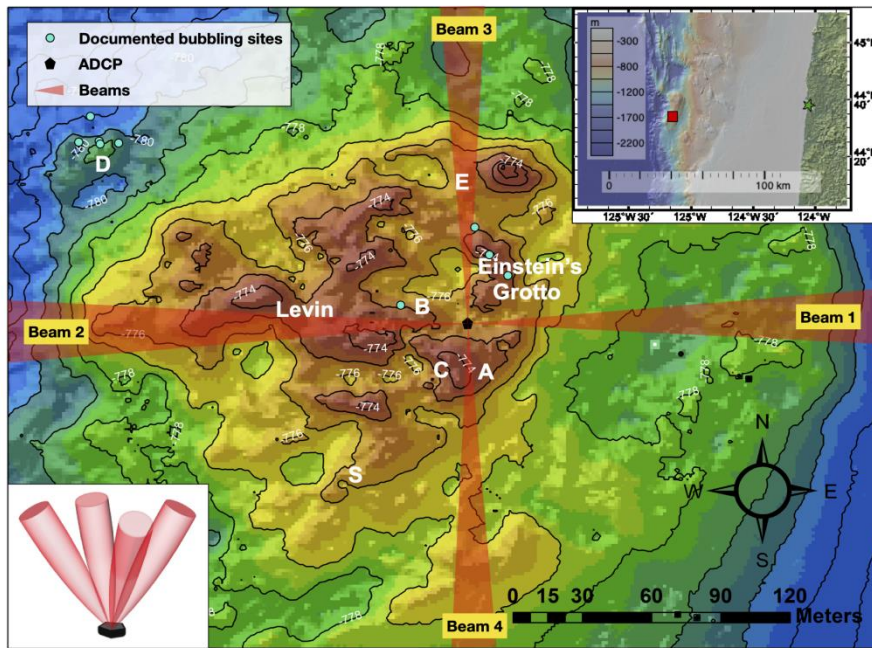


**Figure 1.** Bathymetry map of SHR. Also shown are documented methane emission sites (white lettering), the ADCP (black dot) location, and the ADCP beam orientation. Bathymetric data were obtained during the 2010 Regional Cabled Array survey cruise at SHR using the autonomous underwater vehicle Sentry and R/V Thompson as a courtesy of the University of Washington. The inset map on the top right shows the location of SHR (marked as the red box) relative to Newport, OR (marked as the green star). The inset map is made with GeoMapApp ([www.geomapapp.org](http://www.geomapapp.org)). The inset graphic on the bottom left displays the ADCP beam configuration in 3D. / CC BY / CC BY (source: Ryan et al. 2009).

On the other hand, a recent study at the Clayoquot Slope offshore of British Columbia in 1250 m water depth suggests that falling tides (reducing water load/pressure) could shift the hydrate solubility and induce bubble emissions (Römer et al., 2016). Hence, our study aims to examine the potential tidal impact on the variability of methane bubble emissions for SHR using acoustic data archived by the National Science Foundation's Ocean Observatory Initiative (OOI). This study also evaluates the application of an ADCP as a tool capable of delivering long-term, sustained observations of methane bubble presence.

## 2. Methods

To analyze the long-term variability of methane bubble emissions at SHR, we acquired echo intensity and current velocity data from an upward-looking ADCP. The presence of methane bubbles was inferred using acoustic echo intensity contrast signals (Philip et al., 2016b; Wiggins et al., 2015). Due to the high impedance contrast at the bubble-seawater interface, an ADCP records high signal intensities of echoes returning from the bubbles when the bubbles intersect the ADCP beams (Wiggins et al., 2015). Tidal height was characterized by hourly-averaged seafloor pressure data. To ensure uniformity of the time scale of our data sets, the pressure data were linearly interpolated to the recorded time of the ADCP data using MATLAB. The ADCP also yields information about local currents, including contributions from tides and a more slowly varying background field. This data was used to understand the angle and compass direction of the bubble plume centerline. These data streams are all archived in the OOI data portal. 3.5 months data from 3 March to 23 June 2015 was analyzed in detail to capture the fortnightly variation of tidal height.

### 2.1 ADCP monitoring

According to Philip et al. (2016b) at SHR, a four-beam Teledyne RD Instruments (TRDI) Workhorse Long Ranger 75-kHz ADCP was deployed on the OOI Regional Cabled Array mounted on a benthic frame of medium-powered junction box on 18 September 2014 as shown in Figure 2. The ADCP transmits acoustic pulses at an interval of 2.5s and uses the Doppler frequency shift of backscattered sound to infer the direction and speed of the scattering particles that are assumed to be passively drifting with the ocean current. All four of the ADCP beams are angled at 20° from vertical, passing overhead of several well-documented active seep sites, including Seep B and Einstein's Grotto (Figure 1). Each timestamp of measurements has a vertical resolution of 8 meters, starting 16.73 meters above the seafloor.

### 2.2 Data processing

From the raw ADCP data, we calculate the horizontal current velocities and their corresponding depths. As the raw data were streamed in binary form of beam coordinates, data transformation and rotation are required to match the directions of the data into Earth coordinate direction in order to extract accurate vector data, i.e., the horizontal current velocities. The transformation matrix and the rotation matrix are described in the OOI data product specification (2012). By taking into account of the beams' configuration and the local magnetic declination during the study period, our calculation includes corrections of heading, pitch, roll angle and magnetic

variation for the instrument. For the magnetic variance correction, we use a declination angle of  $15.7573^\circ$  averaged from World Magnetic Model and International Geomagnetic Reference Field over the study period. Depth values corresponding to the ADCP data were calculated using the bin-cell length and minimum measured height above the seafloor. The calculated horizontal velocities were averaged over depth up to 80 m above the seafloor on an hourly basis to derive the tide-resolving current and on a weekly basis to derive the prevailing background current. Directions (in degrees) of the currents were calculated based on the trigonometry of the horizontal velocities. Current vectors are assigned to the principal compass direction as follows:  $350^\circ - 10^\circ$  is north,  $10^\circ - 80^\circ$  is northeast,  $80^\circ - 100^\circ$  is east,  $100^\circ - 170^\circ$  is southeast,  $170^\circ - 190^\circ$  is south,  $190^\circ - 260^\circ$  is southwest,  $260^\circ - 280^\circ$  is west, and  $280^\circ - 350^\circ$  is northwest.

In order to extract bubble signals in echo intensity, we first subtracted a background intensity field and then apply threshold filtering (Figure 2A) to amplify the acoustic contrast signals (Figure 2B). Background intensities were derived by averaging the data from each beam over 3 hours when bubble signals were absent. A threshold of 23 dB was selected, eliminating most of the noise while preserving the acoustic contrast signals (Figure 2B). The remaining isolated strong returns may result from sediments and organisms (zooplankton, fishes). After data cleaning, bubble signals were extracted by counting the number of bin cells of the contrasting intensity signals, which indicate the presence of methane bubbles, at every timestamp throughout the study period (Figure 2C). To further eliminate false detections, we applied a 2-standard-deviation filter of 10 bins for beam 1, 11 bins for beams 2 and 4, and 12 bins for beam 3. Bubble signals from all ADCP beams were then combined for our analysis (Figure 2D).

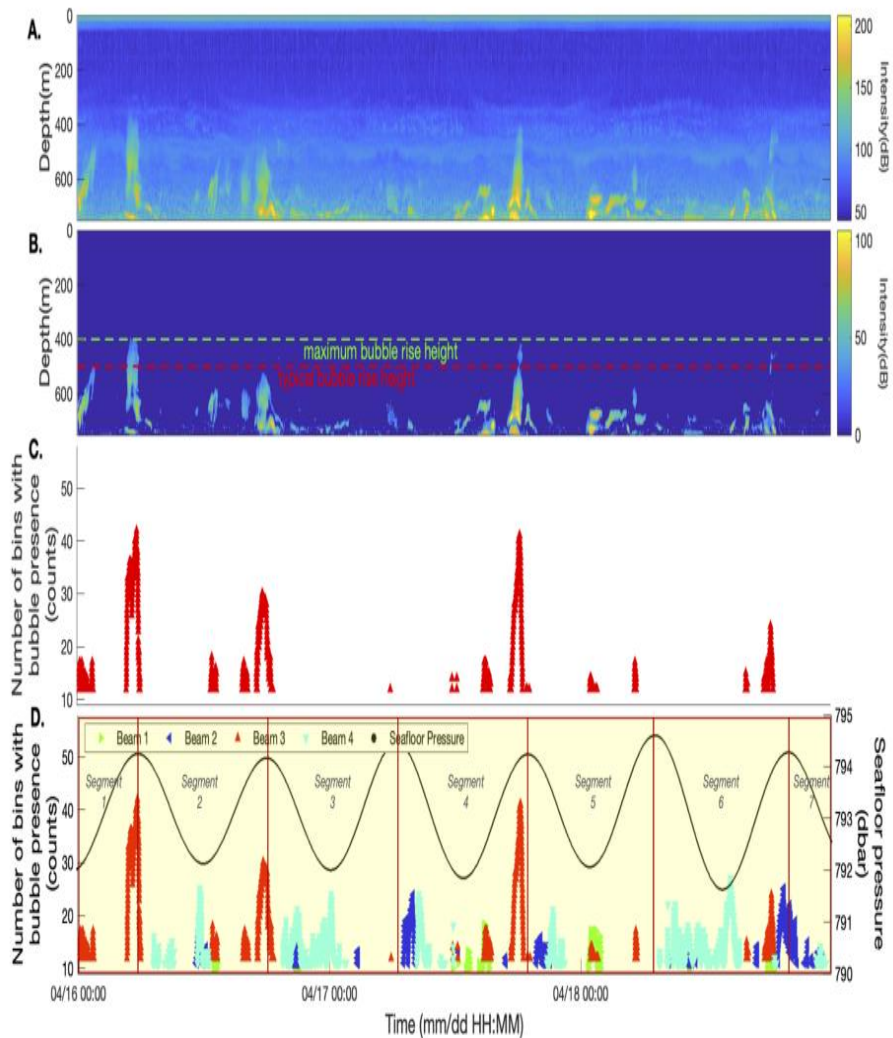


**Figure 2.** Example 3-day record of bubble plume presence as it relates to echo intensity data. All subfigures share the same x-axis displaying time from 16 April to 18 April 2015. (A) Beam-3 transect of raw echo intensity data. (B) Beam-3 transect of echo intensity data with remaining minor noise after removing background intensity and threshold filtering. High intensity plume-like structures signify bubble presence. (C) Beam-3 transect of bubble presence in each vertical bin (y-axis). (D) Relationship between tidal pressure (black line) and bubble presence, combined from all ADCP beams. Vertical lines indicate the 0° = 360° tidal phase.

### 2.3 *Tidal and distribution analysis*

Tidal analysis involves segmenting the bubble signals based on a tidal cycle (Figure 2D) and summing the number of detections that occurred in the same phase of a tidal cycle throughout our study period. A tidal cycle from 0° to 360° phase refers to one period from high tide to high tide using a 0.1° interval. One detection is defined as a bubble signal, regardless of the number of bin counts involved, detected at one timestamp. To prevent bias, periods of NW-flowing prevailing background current and N-NW-dominated tide-resolving current were excluded from our analysis because bubble plumes tended to not intersect the ADCP beams during these periods (discussed in more detail in the Results section). To determine the confidence intervals of the maximum and minimum cumulative detections, we performed t-tests on the detections sampled at identified peak and trough phases. The respective number of degrees of freedom were determined based on an integral time scale defined by the first zero-crossing of the autocorrelation on the cumulative detections, which reveals 55 and 102 phase bins, respectively for the maximum and minimum cumulative detections. With a confidence threshold of 95%, we assessed the statistical significance of the difference in bubble plume presence between its maximum and minimum over the tidal cycle by comparing the estimated lower bound of the maximum detections and the corresponding upper bound of the minimum detections.

Additionally, we performed distribution analysis on the current local speed and bubble rise angles to evaluate the performance of the ADCP in detecting the current-dependent methane bubbles. Assuming a general bubble rise velocity,  $V_{bubble}$ , of 30 cm/s (Rehder et al., 2009), bubble rise angles from the vertical were calculated based on the trigonometric relationship between the speed of tide-resolving current and  $V_{bubble}$ . The resulting distribution of the speed of tide-resolving current and bubble rise angles from vertical was normalized to indicate the relative number of observations. Understanding the behaviour of the local current and bubble rise angles in the area allows us to further assess the capability of the ADCP to detect methane bubbles coming from active seep sites sitting in close proximity (Figure 1).

## 3. Results

### 3.1 *Bubble behaviour at SHR*

Throughout the study period, methane bubbles were detected in all four beams of the ADCP with an episodic and transient behaviour (Figure 2D, Figure 3B). A typical bubble rise height is ~30 bin counts (equivalent to a plume top ~250 m above the seafloor and ~500 m below the sea surface) with a maximum height of ~42 bin counts (~350 m above the seafloor and ~400 m below the sea surface) (Figure 2B). At SHR, the tide-resolving current generally alternates

between the N-NE-NW to S-SE-SW direction (Figure 3A). The tide-resolving current has a mean speed of 9.3 cm/s with a standard deviation of 3.7 cm/s and a 2-sigma limit of 16.8 cm/s (Figure 4.). Comparing  $V_{bubble}$  to the 2-sigma current speed, we found a  $V_{bubble}$  to current speed ratio of  $\sim 1.8$ . The distribution analysis also reveals a mean bubble rise angle (from vertical) of  $15.7^\circ$ , with a standard deviation of  $6.6^\circ$  and a 2-sigma limit of  $28.9^\circ$  (Figure 4.).

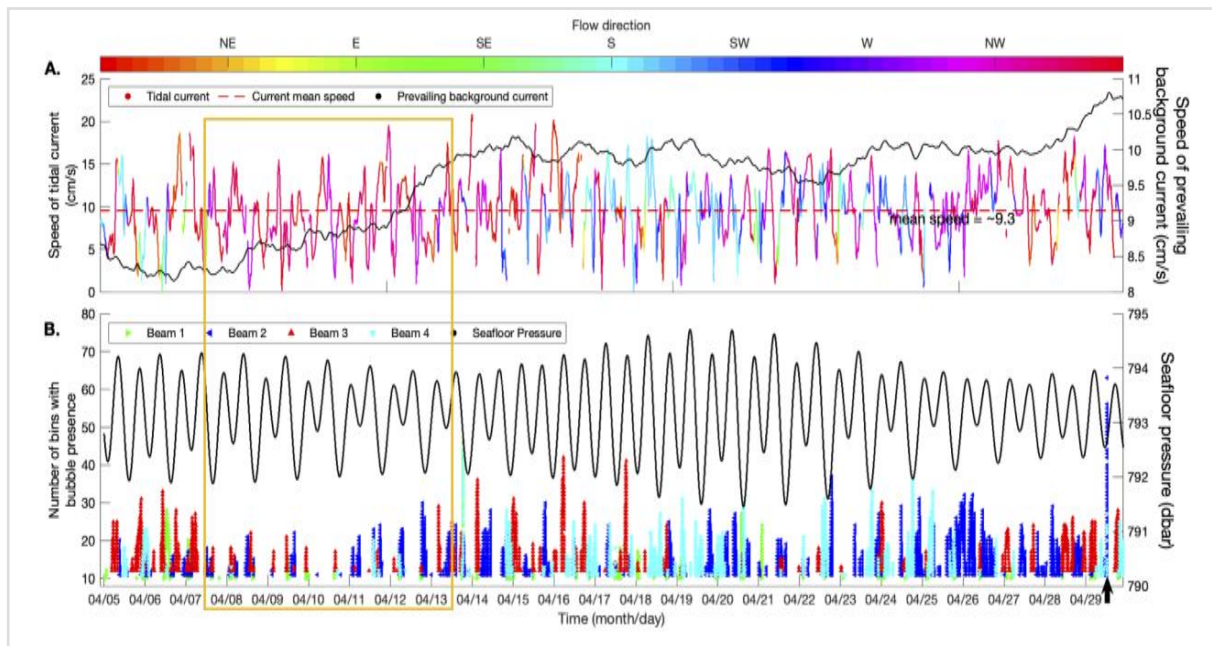


**Figure 3.** (A) Speed of tide-resolving current (coloured by direction) and prevailing background current (black) at SHR. (B) Bubble signals combined from all ADCP beams overlain with seafloor pressure (black). Both subfigures share the same x-axis indicating observation time from 5 to 29 April 2015. The orange box highlights an observed reduction in methane bubble detections during a period with predominantly NW flowing current. The black arrow on 29 April marks a false bubble signal from instrumental error.

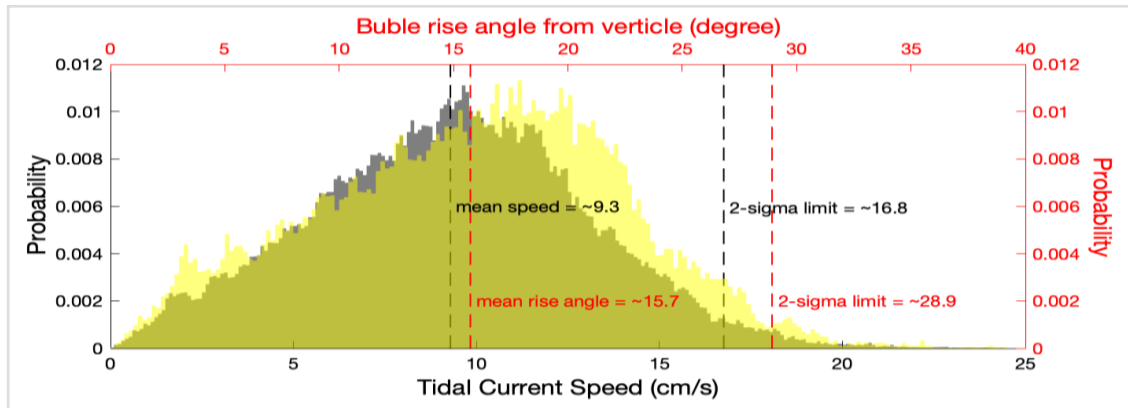


**Figure 4.** Normalized distribution of the speed of tide-resolving current (grey) and bubble rise angles from vertical (yellow).

During the period from 7 to 14 April and from 10 to 18 June, SHR was dominated by northwestward prevailing background current resulting in tidal fluctuations between N and NW (Figure 3A). During these time periods, there were noticeably fewer bubble detections (Figure 3B). This reduction most likely results from the bubble plume failing to intersect the ADCP beams, consistent with the locations of both Seep B and Einstein Grotto to the north of the ADCP. Therefore, these sections of data were excluded from the analysis to prevent potential bias. In addition, false signals resulting from instrumental errors (e.g., Figure 3B) can be found on 5 March, 25 March, 28 March, 29 April, 1 May, 16 May, and 28 May 2015. These errors, unlike bubble signals, extend 75 bins in beams 1 and 2, 66 bins in beam 3, and 57 bins in beam 4.

### ***3.2 Sinusoidal behaviour of cumulative bubble detections over the tidal cycle***

The total number of bubble detections as a function of the tidal phase (referred to as the distribution of cumulative detections) is shown in Figure 5. The distribution resembles a sinusoid with the highest abundance of detections lagging high tide by  $\sim 120^\circ$ . However, some methane bubble plumes were detected throughout the tidal cycle. The highest number of cumulative detections occurs as the tide shifts from high to low. Conversely, as the tide shifts from low to high, a significantly lower number of cumulative detections occurs. The cumulative detection peak occurs at a tidal phase of  $80^\circ$  to  $165^\circ$  with a mean of 429.1 and 95% confidence interval bounds of 421.9 to 436.4. The minimum cumulative detections occurring at the tidal phase of  $276^\circ$  to  $318^\circ$  has a mean value of 151.4 with 95% confidence interval

bounds of 130.9 to 171.8. Comparing the lower bound of detection peak to the upper bound of detection trough, we deduce a detection peak to trough ratio corresponding to a factor of  $\sim 2.5$  in relative abundance. During our study period, the maximum seafloor pressure changes due to tides throughout the study period were  $\sim 3.3$  dbar (Figure 3B).

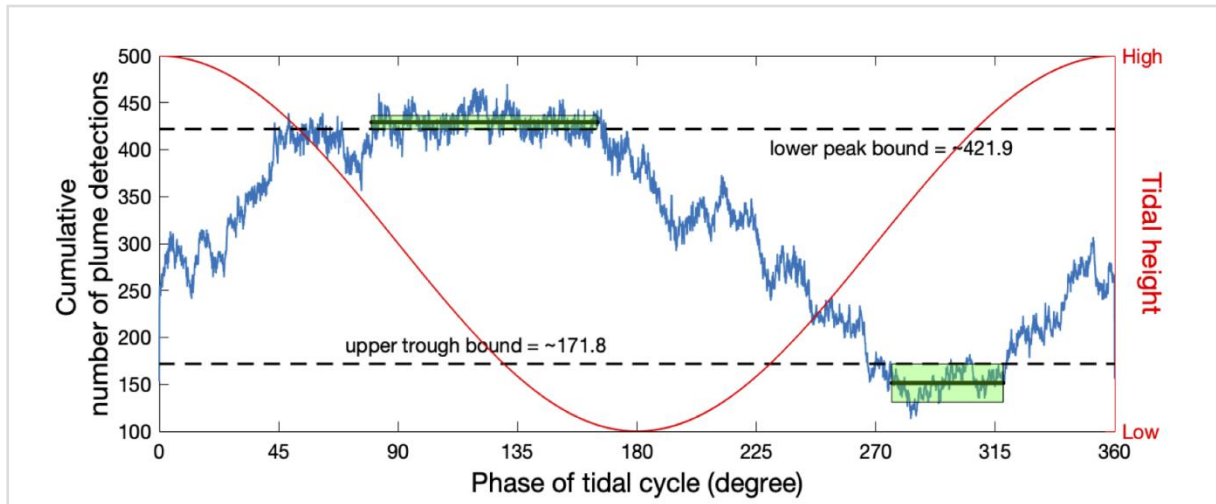


**Figure 5.** Cumulative bubble detections over the tidal cycle from high tide to high tide in  $0.1^\circ$  phase intervals. Green bars at the peak and the trough of the curve show the confidence interval for the mean value (marked by black lines across the green bars) over these time segments taken to represent the maximum and minimum cumulative detections.

## 4. Discussions

### 4.1 Long-term tidal modulation on methane bubble emissions

Tidal analysis reveals a nearly sinusoidal bubble plume response curve that lags  $\sim 120$  degrees from the tidal height (Figure 5), supporting a hypothesis of at least partial tidal control of bubble emissions at SHR. Assuming a transient hydraulic fracturing system at SHR (Daigle, Bangs, and Dugan 2011), decreasing hydrostatic pressure during falling tides could facilitate the bubble flux by promoting the fracturing or reopening of the pre-existing fractures and vice versa.

Further insight into the underlying pore fluid pressure system can be gained by comparing these results to the observations from Clayoquot Slope (Römer et al., 2016), located in a similar geologic setting. With the statistics provided by abundance data over a 3.5-month period, the modulation of plume abundance by tides also emerges at SHR, with up to  $\sim 2.5$  times more plumes at maximum abundance relative to minimum abundance. However,

differences in emission behaviour between SHR and Clayoquot Slope (Römer et al., 2016) suggest a more active pore fluid pressure system at SHR. The primary observations from Clayoquot Slope come from a multi-beam profiling sonar that rotates 360° horizontally every 2 minutes to scan for bubble plumes within a 100 m range. Bubble emissions were typically marked by a clear “onset” time when the echo intensity (averaged over a scan) begins to rise relative to the background (e.g., Figures 6 and 7 in Romer et al., 2016). Approximately 88% of these onset events occur during the falling tide. The strongest average echo intensity follows several hours later, typically during the rising tide. Our data cannot be directly compared with that of Römer et al., 2016, since we use a binary metric indicating the presence or absence of a plume, irrespective of its intensity. However, at SHR we see significant bubble plume presence throughout the tidal cycle (Figure 3B and Figure 5). Furthermore, we would expect more markers of presence during times of peak emission, and at Clayoquot Slope these maxima are centered on the rising tide. In contrast, at SHR the rising tide corresponds to a lower abundance of observed plumes. Thus, our observations suggest that the onset of enhanced bubble activity at SHR occurs earlier in the tidal cycle than Clayoquot Slope, building to maximum emission during the falling tide.

At Clayoquot Slope, three different phases of emission behaviour were observed between June 2012 and July 2013: (1) short activity up to hours where onset is linked to falling tides as just discussed, (2) transient activity and inactivity up to days, and (3) continuous activity up to weeks (Römer et al. 2016). Consistent with observations in previous studies (Philip et al. 2016a; Riedel et al. 2018), emission behaviour at SHR is more transient and episodic (Figure 3B). The relationship with tidal forcing is less regular and only emerges in the cumulative distribution over a multi-month record. For this reason, and because of the likely difference in phasing within the tidal cycle, we suspect that unlike Clayoquot Slope in which tidal pressure forcing is the major control, the bubble emission behaviour at SHR is most likely dependent on both the tidal pressure forcing, as well as variations in the underlying pore fluid pressure.

By generalizing a dynamic equilibrium between the seafloor pressure and the pore fluid pressure with the assumption of a hydraulic fracturing system (Daigle, Bangs, and Dugan 2011) and with continuous fueling of gas bubbles below the MHSZ, we present a conceptual model with a cycle of 4 phases of bubble emissions at SHR (Figure 6). If sediment pore pressure is low during the phase of high tide (high seafloor pressure), there is a low probability that the effective overlying stress will be overcome by pore pressure. Therefore, bubble emissions are less likely (Phase 1); as bubble pressure builds up within the sediment, the likelihood of bubble

emissions increases. However, due to high hydrostatic seafloor pressure inhibition, bubble emissions frequency is limited to a moderate level during high tide (Phase 2). The highest frequency of bubble emissions occurs when tidal pressure decreases (Phase 3). This increased bubble emission during the falling tide causes a reduction of the excess pore pressure built up during the inhibition phase, leading to a subsequent reduction in emissions to a moderate level (Phase 4). The cycle starts over again when tidal pressure begins to increase, inhibiting bubble flux from the seafloor and allowing excess pressure to build, fueled by continuous release from below the MHSZ.

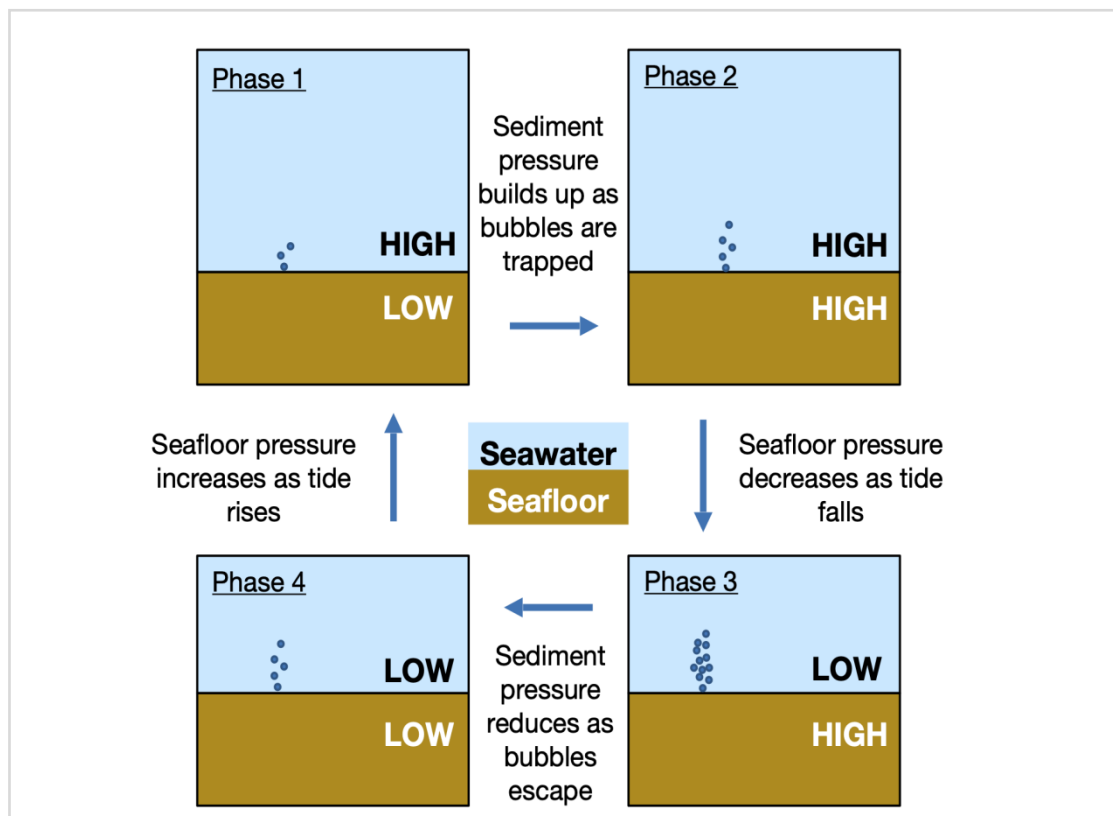


**Figure 6.** Schematic model of long-term bubble emission behavior at SHR. Higher bubble density indicates higher tendency of bubble emissions. Diagrams are not to scale.

#### 4.2 An adequate instrument for long-term analyses

The ADCP at SHR has demonstrated its reliability in capturing bubbles from close-distance sources, such as Seep B and Einstein’s Grotto. Overall, we found a similar maximum bubble plume rise height of ~350 m to previous work using high-resolution ship-based sonar (Philip et al. 2016a), lending confidence that the upward-looking ADCP captures most of the bubble plume signal. Generally, the performance of an ADCP in detecting bubble plumes depends on

the probability of bubbles intersecting the fixed ADCP beams (Figure 1). Because bubble transport in water is current-dependent (Heeschen et al. 2004), further controlling the centerline angle of the bubble plume, bubble detection by an upward-looking ADCP is dependent on the direction of the tide-resolving current, as well as the prevailing background current (Figure 3A). Such dependence on the current direction has both limited and enhanced bubble detection at SHR. With Seep B and Einstein Grotto's located to the north of the ADCP, the bubble plume is less likely to intersect with the ADCP beam during periods of N-NW prevailing background current, causing reduced bubble detection between 7 to 14 April (Figure 3).

On the other hand, the bubble plume is very likely to intersect with the ADCP beams most of the time, as the tidally modulated current more commonly fluctuate between N-NE-NW and S-SE-SW at SHR (Figure 3A). In addition, with a high  $V_{bubble}$  to current speed ratio and low bubble rise angles of  $<30^\circ$  from vertical (Figure 4), close-distance bubbles are highly likely to intersect an ADCP beam, if not at a shallow height. At a height in which the beams have wider widths as the current disperses the bubble plume laterally. With that, we assert the bubble signals observed in the ADCP at SHR are reliable for resolving the statistical relationship of bubble plume presence and the tidal cycle. Understanding how the current ocean variations may limit detection in a given setting allows for cleaner signal extraction, in this case, because we can eliminate potential bias during periods of N-NW prevailing flow.

Unlike some previous studies which use error velocity as an indicator of bubble presence (Philip et al. 2016b; Wiggins et al. 2015), our study (along with that of Römer et al. 2016) demonstrates how echo intensity can be a reliable alternative bubble indicator with minor limitations. Examples of limitations observed in our data include (1) remaining random background noise (Figure 2B) and (2) false signals from instrumental errors (figure 3B). These limitations do not affect the overall result of our study since it is based on the cumulative presence in a given phase of the tide over many cycles. Because the remaining random background noise is mostly comprised of high returns spanning a small number of bin counts, it can largely be eliminated by applying a 2-standard-deviation filter to the extracted bubble signals. Similarly, unidentified instrumental errors only make up a minute fraction of time out of the 3.5-month record, rendering their contribution insignificant. Hence, bubble signals derived from echo intensity, with appropriate data-cleaning, can be optimized for long term analyses.

This application of an ADCP to bubble plume detection yields insight about important considerations for future applications, including an understanding of bubble plume sources, current local variability, and beam geometry. For seep monitoring, due to the fixed beam

geometry, an ADCP performs best with bubble sources located in close proximity. Assuming a bubble rise velocity greater than the current speed, and ADCP should be deployed such that the bubble rising angle from vertical is similar to or lower than the ADCP beam angle. In terms of the local ocean current environment, strong variability, including tidal flow, enhances the performance of monitoring overall, as there is a higher probability of bubbles intersecting the ADCP beams. Deployment of a secondary, mechanical current meter may allow for greater accuracy in measuring the bottom current speed and direction without the acoustic “noise” from bubbles. In the case of bubbles escaping from the beam detection due to the limitation of an ADCP’s geometry, deploying another ADCP with a geometry of opposite directions would allow detections of bubbles that escape from the first ADCP. Therefore, for future studies, having multiple ADCP’s coupled with a current meter that is judiciously placed would allow for the high probability of the detection of plumes during all relevant fluid flow regimes with greater accuracy.

#### **4.3 *Future possibilities for research into mechanisms controlling bubble emissions***

Although our study reveals tidal modulation of bubble emission at SHR, validation of the mechanism controlling this behaviour as well as the observed discontinuity in emissions requires a better understanding of the behaviour of pore fluid pressure and hydrate stability in response to hydrostatic pressure changes coupled with the potential for influence from temperature variations and earthquakes. The study of such subtleties is possible through conducting a similar experiment with analyses of real-time data over the longer term, transmitted via BluComm or a cabled sensor array, from an instrumentation array that includes temperature probes, short-period seismometers, and pore fluid pressure sensors. Greater resolution of bubble emissions is likely attainable with the underwater deep-sea sonars. In fact, pore fluid pressure sensors aside, the current cabled instrumentations at SHR includes broadband and short-period seismometers, benthic flow sensors, a mass spectrometer, a pressure sensor, a digital still camera, an Osmo fluid sampler, an ADCP, a current meter and deep-sea sonars. By identifying a novel experimental configuration and taking advantage of the long-term instrumentations at SHR, the possibilities exist for a comprehensive understanding of hydrate (and bubble emissions) sensitivity to varying hydrostatic pressure, temperatures and earthquakes. Such comprehensive analyses may provide insights into the mechanisms attributing the discontinuity of methane bubble emissions and the underlying hydrate stability in the seafloor.

## 5. Conclusions

Our study has demonstrated, with some limitations, how an upward-looking ADCP can be an adequate instrument for long-term studies of bubble emissions from gas seep sites. Despite the lack of a cleanly repeating tidal signal, high temporal resolution ADCP data over ~3.5 months reveals a statistical relationship between bubble plume presence and tidal phase, implying a significant tidal impact on methane emissions at SHR. Bubbling behaviour throughout the tidal cycle at SHR suggests a tidally modulated dynamic equilibrium between the seafloor pressure and the pore fluid pressure. Hydrostatic pressure changes due to tides promote or inhibit hydraulic fracturing in the seafloor, leading to bubble emissions. Future quantification of carbon output from marine hydrate reservoirs should consider the tidal impact on methane seeps. Additional, comprehensive analyses with high-resolution data over a longer time period integrating multiple factors characterizing the emission behaviour and hydrate stability are required to better quantify the discontinuity of methane bubble emission at SHR, which may impact understanding on the methane seeps' contribution to the global atmospheric carbon budget.

## Acknowledgements

Data were obtained from instruments on NSF's Regional Cabled Array, a component of the OOI, and are available at NSF OOI's Comprehensive Large Array Data Stewardship System. Research was conducted through the courses of OCEAN 443, OCEAN 444, and OCEAN 445 at the University of Washington School of Oceanography. This work is supported by the Mary Gates Endowment for Students. Thank you to the UW VISIONS' 18 at-sea program (Deborah Kelley), which provided the first direct view of SHR and an introduction to this seep site. Thank you to UW School of Oceanography (John Delaney, Brendan Philip, Arthur Nowell, Paul Johnson, and Deborah Kelley) for undergraduate research support.

## References

- Archer, D., 2007. "*Methane Hydrate Stability and Anthropogenic Climate Change*". *Biogeosciences*, 4(4), :521-544.
- Bangs, Nathan L. B., Robert J. Musgrave, and Anne M. Tréhu. 2005. "Upward shifts in the southern Hydrate Ridge gas hydrate stability zone following postglacial warming, offshore Oregon." *Journal of Geophysical Research. Solid Earth*, Volume 110, Issue B3 <https://doi.org/10.1029/2004JB003293>

- Beaudoin, Yannick C., W. Waite, R. Boswell, and S. R. Dallimore. 2014. “*Frozen Heat: A UNEP Global Outlook on Methane Gas Hydrates*”. Vol. 2. Norway: United Nations Environmental Programme, GRID-Arenda.
- Daigle, H., Bangs, N.L. and Dugan, B., 2011. “*Transient Hydraulic Fracturing and Gas Release in Methane Hydrate Settings: A Case Study from Southern Hydrate Ridge*”. *Geochemistry, Geophysics, Geosystems*, 12(12).
- Etiopie, G. and Milkov, A.V., 2004. “*A New Estimate of Global Methane Flux from Onshore and Shallow Submarine Mud Volcanoes to The Atmosphere*”. *Environmental Geology*, 46(8), :997-1002.
- Hautala, S.L., Solomon, E.A., Johnson, H.P., Harris, R.N. and Miller, U.K., 2014. “*Dissociation of Cascadia Margin Gas Hydrates in Response to Contemporary Ocean Warming*”. *Geophysical Research Letters*, 41(23), :8486-8494.
- Heeschen, K.U., Collier, R.W., de Angelis, M.A., Suess, E., Rehder, G., Linke, P. and Klinkhammer, G.P., 2005. “*Methane Sources, Distributions, and Fluxes from Cold Vent Sites at Hydrate Ridge, Cascadia Margin*”. *Global Biogeochemical Cycles*, 19(2).
- Johnson, H. Paul, Una K. Miller, Marie S. Salmi, and Evan A. Solomon. 2015. “*Analysis of Bubble Plume Distributions to Evaluate Methane Hydrate Decomposition on the Continental Slope.*” *Geochem., Geophys., Geosyst.* 16 (11): 3825-3839.
- Johnson, J.E., Goldfinger, C., Tréhu, A.M., Bangs, N.L.B., Torres, M.E. and Chevallier, J., 2006. “*North-South Variability in The History of Deformation and Fluid Venting Across Hydrate Ridge, Cascadia Margin*”.
- Katz, M.E., Cramer, B.S., Mountain, G.S., Katz, S. and Miller, K.G., 2001. “*Uncorking the Bottle: What Triggered the Paleocene/Eocene Thermal Maximum Methane Release?*”. *Paleoceanography*, 16(6), :549-562.
- Liu, L., Ryu, B., Sun, Z., Wu, N., Cao, H., Geng, W., Zhang, X., Jia, Y., Xu, C., Guo, L. and Wang, L., 2019. “*Monitoring and Research on Environmental Impacts Related to Marine Natural Gas Hydrates: Review and Future Perspective*”. *Journal of Natural Gas Science and Engineering*, 65, :82-107.
- McGinnis, D., Greinert, J., Artemov, Y., Beaubien, S.E. and Wuest, A., “*Fate of Rising Methane Bubbles 3225 in Stratified Waters: How Much Methane Reaches the Atmosphere*”. *Journal of Geophysical Research: Atmospheres*, 111.
- National Research Council. 2009. *Realizing the Energy Potential of Methane Hydrate for the United States*. Washington, D.C.: National Academies Press.

- NSF Ocean Observatories Initiative Data Portal (Tidal Seafloor Pressure Data file: RS01SUM1-LJ01B-09-PRESTB102, 3 March to 23 June 2015; Accessed December 1, 2018). <http://ooinet.oceanobservatories.org>.
- NSF Ocean Observatories Initiative Raw Data Archive (Velocity Profiler Raw data file: RS01SUM2-MJ01B-12-ADCPSK101, 3 March to 23 June 2015; Accessed December 1, 2018). <https://oceanobservatories.org/data/raw-data/>.
- OOI (2012). *Data Product Specification for Velocity Profile and Echo Intensity* (Document Control Number 1341-00750). Available at <https://oceanobservatories.org/wp-content/uploads/2015/10/>.
- Philip, B.T., Denny, A.R., Solomon, E.A. and Kelley, D.S., 2016. “*Time-Series Measurements of Bubble Plume Variability and Water Column Methane Distribution Above Southern Hydrate Ridge, Oregon*”. *Geochemistry, Geophysics, Geosystems*, 17(3): 1182-1196.
- Philip, B.T., Kelley, D.S., Solomon, E.A. and Delaney, J.R., 2016, September. “*Monitoring Methane Emissions at Southern Hydrate Ridge Using an OOI Cabled Array Acoustic Doppler Current Profiler*”. In OCEANS 2016 MTS/IEEE Monterey: pp. 1-5. IEEE.
- Rehder, G., Leifer, I., Brewer, P.G., Friederich, G. and Peltzer, E.T., 2009. “*Controls on Methane Bubble Dissolution Inside and Outside the Hydrate Stability Field from Open Ocean Field Experiments and Numerical Modeling*”. *Marine Chemistry*, 114(1-2): 19-30.
- Riedel, M., Scherwath, M., Römer, M., Veloso, M., Heesemann, M. and Spence, G.D., 2018. “*Distributed Natural Gas Venting Offshore Along the Cascadia Margin*”. *Nature communications*, 9(1): 1-14.
- Römer, M., Riedel, M., Scherwath, M., Heesemann, M. and Spence, G.D., 2016. “*Tidally Controlled Gas Bubble Emissions: A Comprehensive Study Using Long-Term Monitoring Data from the NEPTUNE Cabled Observatory Offshore Vancouver Island*”. *Geochemistry, Geophysics, Geosystems*, 17(9): 3797-3814.
- Ruppel, C.D., 2011. “*Methane Hydrates and Contemporary Climate Change*”. *Nature Education Knowledge*, 2(12): 12.
- Ryan, W.B., Carbotte, S.M., Coplan, J.O., O'Hara, S., Melkonian, A., Arko, R., Weissel, R.A., Ferrini, V., Goodwillie, A., Nitsche, F. and Bonczkowski, J., 2009. “*Global Multi-Resolution Topography Synthesis*”. *Geochemistry, Geophysics, Geosystems*, 10(3).
- Solomon, E.A., Kastner, M., Jannasch, H., Robertson, G. and Weinstein, Y., 2008. “*Dynamic Fluid Flow and Chemical Fluxes Associated with a Seafloor Gas Hydrate Deposit on*

- The Northern Gulf of Mexico Slope*". Earth and Planetary Science Letters, 270(1-2): 95-105.
- Torres, M.E., McManus, J., Hammond, D.E., De Angelis, M.A., Heeschen, K.U., Colbert, S.L., Tryon, M.D., Brown, K.M. and Suess, E., 2002. "*Fluid and Chemical Fluxes in and Out of Sediments Hosting Methane Hydrate Deposits on Hydrate Ridge, OR, I: Hydrological Provinces*". Earth and Planetary Science Letters, 201(3-4): 525-540.
- Tréhu, A.M., 2006. "*Gas Hydrates in Marine Sediments: Lessons from Scientific Ocean Drilling*". Oceanography, 19, :124-142.
- Tryon, M.D., Brown, K.M., Torres, M.E., Tréhu, A.M., McManus, J. and Collier, R.W., 1999. "*Measurements of Transience and Downward Fluid Flow Near Episodic Methane Gas Vents, Hydrate Ridge, Cascadia*". Geology, 27(12): 1075-1078.
- Wiggins, S.M., Leifer, I., Linke, P. and Hildebrand, J.A., 2015. "*Long-Term Acoustic Monitoring at North Sea Well Site 22/4b*". Marine and Petroleum Geology, 68, :776-788.